Nuclear Inst. and Methods in Physics Research, A 875 (2017) 16–20

Contents lists available at ScienceDirect

Nuclear Inst. and Methods in Physics Research, A

journal homepage: www.elsevier.com/locate/nima

The planispherical chamber: A parallax-free gaseous X-ray detector for imaging applications

F.M. Brunbauer [a,b,*], E. Oliveri [a], F. Resnati [a], L. Ropelewski [a], F. Sauli [a], P. Thuiner [a], M. van Stenis [a]

[a] CERN, 385 Route de Meyrin, 1217 Meyrin, Geneva, Switzerland
[b] Technische Universität Wien, Karlsplatz 13, 1040 Wien, Austria

ARTICLE INFO

Keywords:
Gaseous detector
Parallax-free
Gaseous electron multiplier
GEM
Crystallography
Fluorescence

ABSTRACT

Crystallography or X-ray fluorescence experiments which require good signal to noise ratios and high position resolution can take advantage of the outstanding signal amplification capabilities of MicroPattern Gaseous Detectors (MPGDs) such as Gaseous Electron Multipliers (GEMs) coupled with the position resolution achieved by optical readout realized with CCD or CMOS cameras. Increasing the detection probability of incident radiation with thicker drift volumes in these detectors leads to a spatial resolution-limiting parallax error when employing parallel electric field lines in the drift region.

We describe a new GEM-based detector concept, consisting of a cathode, GEM electrodes and field shaping rings suitably segmented and powered to create a radial electric field, thus minimizing the parallax error. A CCD camera is used to record scintillation light originating from charge multiplication in the high field of the GEM holes in an Ar/CF_4 (80/20%) gas mixture. Assembled as pinhole camera, the device permits to obtain high detection efficiencies for soft X-rays, exempt from the parallax error intrinsic in the use of standard gaseous detectors with thick conversion layers. The use of several GEMs in cascade allows for high charge multiplication factors. Switching from straight to radially focused drift field lines, a significant reduction of the parallax error as well as an increased signal-to-noise ratio were achieved, effectively paving the way for applications such as X-ray crystallography realized with optically read out GEMs.

1. Introduction

Structural analysis methods such as crystallographic studies by X-ray diffraction or X-ray fluorescence imaging require radiation detectors, which can combine excellent position resolution with strong signals. MicroPattern Gaseous Detectors (MPGDs) such as Gaseous Electron Multipliers (GEMs) [1] have been proven to allow for strong signal amplification as well as a good inherent position resolution [2] and are employed in a number of fields ranging from high energy physics [3,4] and imaging applications [5,6] to medical radiography [7,8].

Recent developments in imaging sensors have made optical readout of MPGDs an attractive concept for achieving high position resolution coupled with reduced sensitivity to electronic noise and a simple way of obtaining visual representations of ionizing radiation without the need for complex front-end electronics and extensive reconstruction algorithms. Several studies and developments demonstrate the potential of the combination of optical readout with MPGDs [9–11].

In the application of gaseous detectors for X-ray crystallography or X-ray fluorescence, a limiting factor is the value of the absorption length, which increases with photon energy. The ensuing lower efficiency can be compensated by the use of thick conversion layers; for non-parallel photon fields, however, this introduces a substantial parallax error resulting in loss of resolution. This error is caused by the uncertainty in the depth of the initial ionization in the gas by the incident radiation in the case of parallel electric field lines as shown schematically in Fig. 1(a).

In an Ar-filled detector at 1 bar, at an incidence angle of ten degrees to the normal, the parallax error is 5 mm for a 3 cm drift gap, while providing a modest 20% efficiency for 10 keV X-rays. This has to be compared to the sub-mm intrinsic resolution of modern MPGDs [12]. Operating at high pressures or with heavier gases such as Kr or Xe reduces these errors but results in technical complications and higher costs.

The parallax error can be reduced by the use of special cathode geometries but remains substantial [13]. A way to overcome the

* Corresponding author at: CERN, 385 Route de Meyrin, 1217 Meyrin, Geneva, Switzerland.
E-mail address: florian.brunbauer@cern.ch (F.M. Brunbauer).

http://dx.doi.org/10.1016/j.nima.2017.08.060
Received 19 May 2017; Accepted 31 August 2017
Available online 6 September 2017

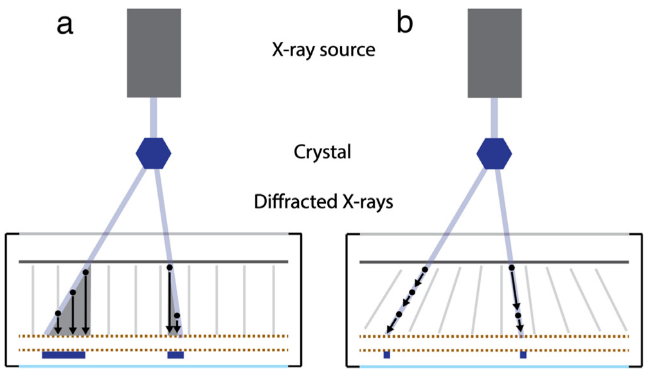

Fig. 1. Parallax error causes broadening of signal in GEM-based detector with thick drift volume in X-ray crystal diffraction measurement. (a) Parallel drift field lines result in signal broadening. (b) Radially focused drift field lines mitigate the parallax error and preserve position resolution.

problem is to record the time of the conversion from the gas scintillation emitted in the primary interaction and deduce the penetration depth from a measurement of the drift time of the ionization electrons. Owing to the small photon yield of the process, this has been successfully achieved only in Xe-filled devices such as the scintillating drift chamber, consisting of a gaseous counter coupled to a photomultiplier detecting both the primary fluorescence and the secondary emission during charge multiplication in high fields [14]. A similar approach constitutes the basis for detection of small energy losses in liquid-Xe time projection chambers designed for rare events physics [15]. The development of GEM detectors with a thin-layer CsI photocathode deposited on the electrodes, sensitive to UV photons above 5.8 eV, has permitted to demonstrate the possibility of recording the time of conversion and detecting the primary scintillation as well as the main ionization charge within the same structure [16]. Requiring a Xe filling, however, the approach remains limited in applications.

Alternatively, the parallax error can be mitigated by constructing a detector with radially focused electric field lines in the conversion volume between a semi-spherical cathode and a mesh. In this case, the ionization charge can subsequently be transferred to a planar amplification structure using a multiwire proportional chamber [17]. Such a device named a spherical drift chamber was successfully used for many years in the analysis of macromolecules by studying X-ray diffraction patterns [18].

A recent development makes use of thermally deformed spherical GEM electrodes to achieve radially focused drift field lines and minimize parallax-induced broadening [19]. In addition to manufacturing difficulties, the spherical GEM foils require specially designed readout electronics and are not ideally suited for optical readout.

While all these previous developments have employed electronic readout and were limited by manufacturing or technical difficulties, we present an experimental demonstration of the simplicity and versatility of combining a planispherical GEM detector achieving radially focused drift field lines with segmented electrodes as shown in Fig. 1(b) with optical readout to realize a fast and stable detector with minimized parallax-induced broadening, which is well-suited for X-ray diffraction and fluorescence imaging applications. Furthermore, the presented design also allows for adjustable focal lengths for increased flexibility and universality.

2. Experimental methods

Two segmented GEM foils, a segmented cathode together with a segmented field shaper and a borosilicate viewport below the second GEM were assembled around a circular POM frame forming the gas volume of the detector, as shown in Fig. 2(a). The segmented GEMs feature five separated ring-shaped electrodes, a circular active region with a diameter of 10 cm and holes with a diameter of 70 μm at 140 μm pitch and were manufactured with a double mask etching technique. The connections to the individual electrodes were routed asymmetrically to the outside of the active detector volume to allow for a minimal dead area due to solid Cu tracks when operating in a dual-GEM setup. Fig. 2(b) shows a schematic representation of the employed GEM layout; Fig. 2(c) is a picture of the assembled detector.

The ring-shaped segments of the cathode and of the first GEM as well as the field shaper were connected at graded potentials with values determined so that the field lines in the 25 mm thick drift region radially focus on a point 10 cm away from the cathode. Designing each ring with a different width with thinner rings on the outside, a voltage divider with equal resistors between sectors could be used to power the GEMs. Resistor chains with selected resistor combinations and multiple power supply channels were used to bias all sectors with the potentials determined by simulation to result in optimized radial drift field lines, while retaining the flexibility to modify amplification and transfer fields easily. While the segments of cathode, field shaper and first GEM were all at different potentials, the second GEM was used in planar mode, i.e. all segments at the same potential, since only a small and correctable distortion is induced by the moderate nonuniformity of the transfer field between the two GEMs. Use of two GEM foils in cascade permits to obtain large photon yields at moderate operating voltages, thus increasing the safety and stability of operation [1].

A six megapixel CCD camera with a cooled image sensor featuring 4.54×4.54 μm^2 pixels was placed in a light shielding tube below the borosilicate viewport facing the bottom of the second GEM and used to record the secondary scintillation light emitted during avalanche amplification in the holes of the second GEM. The detector was operated in open gas flow mode with an Ar/CF_4 (80/20% by volume) gas mixture at 1 bar since CF_4 has a secondary scintillation spectrum [20], which closely matches the quantum efficiency of the employed CCD camera.

To verify gain uniformity across the active area and compare it to the case of a standard drift field configuration, flood exposures with parallel incident radiation irradiating the whole GEM area were taken

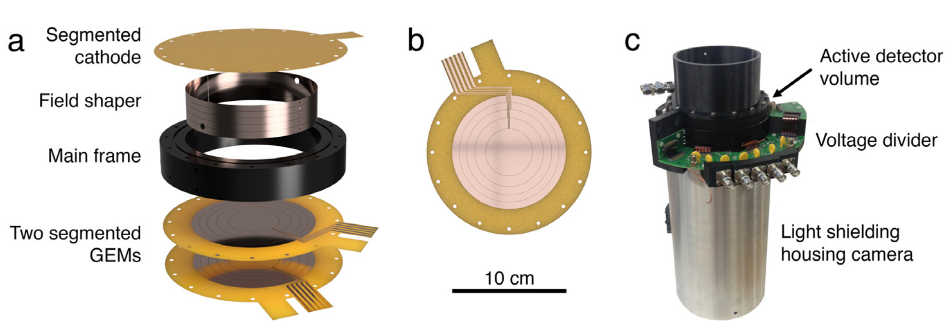

Fig. 2. (a) Exploded view of active detector volume with main frame, segmented cathode, two segmented GEMs and field shaper. (b) Layout of segmented GEM with five ring-shaped electrodes and circular active region with a diameter of 10 cm. (c) Fully assembled detector with light shielding tube housing the CCD camera below the active detector volume as well as the voltage divider and distribution PCBs.

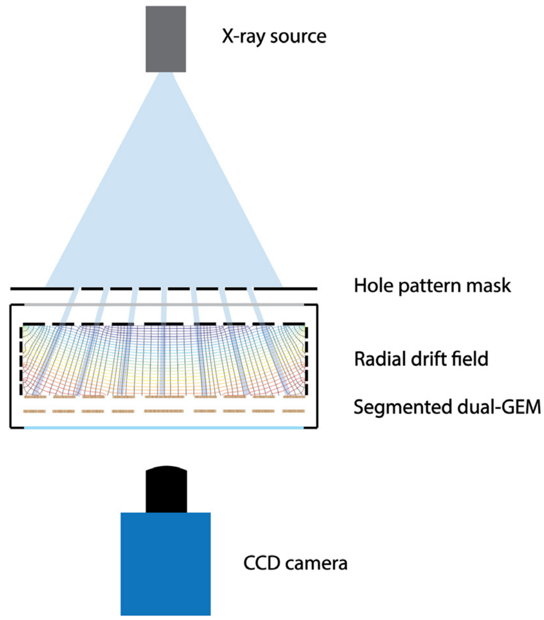

Fig. 3. Schematic of setup used to compare hole pattern images when using straight or radial drift fields. The drift field lines in radial field configuration, focused at a source 10 cm above the cathode, are shown in the drift volume (computed with COMSOL software [21]). A CCD camera below the second GEM records secondary scintillation light.

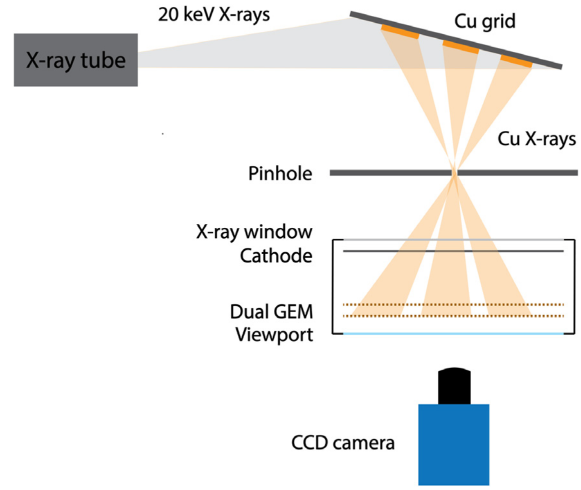

Fig. 4. Schematic of X-ray fluorescence setup. A Cu grid is irradiated with 20 keV X-rays and the emitted characteristic Cu X-rays are focused by a pinhole in the focal point of the radial drift field lines of the detector.

with a Cu X-ray tube. To demonstrate the parallax-free operation of the planispherical detector and as shown in Fig. 3, a setup consisting of a point-like ^{55}Fe X-ray source placed in the focal point of the radial drift field lines irradiating a 0.2 mm thick Cu disk with 0.5 mm diameter holes spaced by 5 mm or 10 mm in a crosshair pattern was used to demonstrate the difference in the detector response when using straight or radial drift field configurations. Also, simple fluorescence images were taken with a grid of vertical and horizontal Cu lines spaced by 5 mm irradiated with 20 keV X-rays positioned at an angle in front of the detector with a pinhole in the focal point of the radial drift field lines for focusing the emitted characteristic Cu X-rays, as shown schematically in Fig. 4.

3. Results and discussion

The uniformity of the gain and electron collection across the active area of the GEM was verified by flood exposures with parallel Cu X-rays. A comparison of flood exposures for straight and radial drift fields is shown in Fig. 5.

When the GEMs are operated with the ring-shaped electrodes connected together to create a straight drift field, the signal intensity expressed as the grayscale value in the shown CCD images across the active area of the GEM is approximately uniform with the exception of vignetting and some nonuniformity of the beam profile. When using a radial drift field, the potential differences between neighboring ring-shaped electrodes create an intensity gradient across each electrode, which peaks at the inner border and has a minimum at the outer one. This can be attributed to unbalanced electron collection in the vicinity of the insulating regions between electrodes, which are at different potentials. To create a radial drift field, electrodes on the outside are biased more positively, which leads to electrons drifting towards the insulating regions between electrodes being preferably collected by the outer electrode. A horizontal line profile of the flood exposure in radial field configuration as shown in Fig. 5(b) across the active area of the GEM is shown in Fig. 6.

The distortions on the edges of the sectors arise from the discrete voltage steps between individual segments of the electrodes. Employing image processing algorithms or a greater number of narrower electrode segments, these distortions could be corrected for or minimized.

A standard drift field with parallel electric field lines perpendicular to the cathode results in significant distortions in the representation of a crosshair hole pattern, as shown in Fig. 7(a). When biasing each ring-shaped electrode individually and creating radial drift field lines

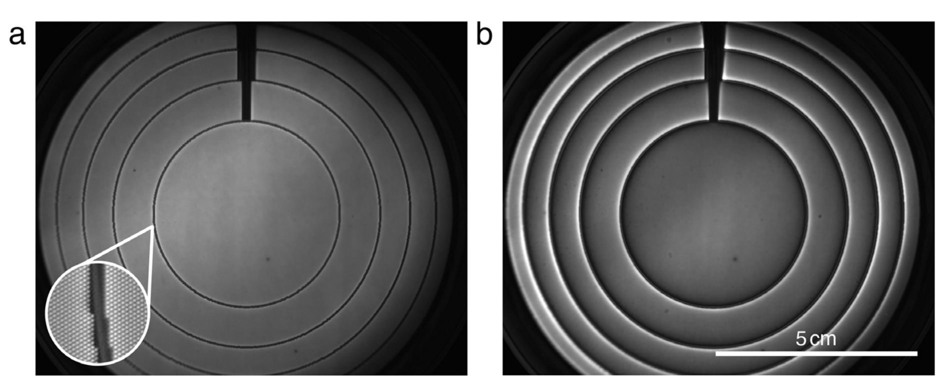

Fig. 5. Flood exposures with parallel Cu X-rays recorded with 1 s exposure without binning. Dark rings are due to the 200 μm wide electrical insulation gaps between sectors, while the dark region at the top originates from solid Cu connection tracks to the sectors. (a) For the case of all ring-shaped sectors connected together, the gain of the GEM is uniform across the active region. Inset: the holes of the second GEM are clearly visible. (b) For a radial drift field, the grayscale value varies across each sector with a higher value at the inner border of each sector.

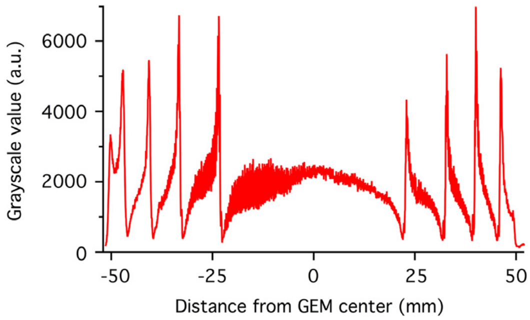

Fig. 6. Horizontal line profile across flood exposure taken with radial drift field.

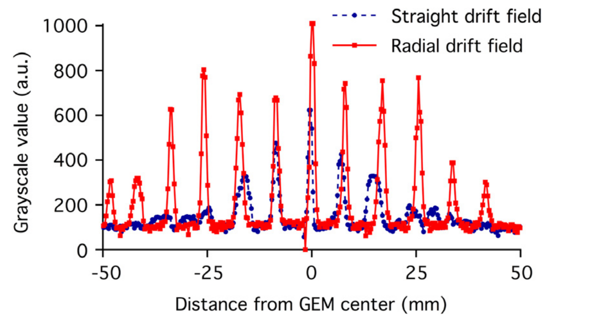

Fig. 8. Horizontal line profiles of the grayscale value along the central line of holes in an image of a hole pattern taken with straight drift field lines (dashed line) compared to the case of radial drift field lines focused at the X-ray source (solid line).

focused at the location of the radiation source, the parallax error is minimized and a non-dispersive and better focused representation of the hole pattern is obtained, as shown in Fig. 7(b).

Both images in Fig. 7 are shown with the same grayscale value range. The significantly better signal-to-noise ratio and the fact that it is preserved in off-center regions of the active area in the image obtained with a radial drift field is due to the reduced broadening of the spots of the hole pattern mask.

Horizontal line profiles of the grayscale value in the two images shown in Fig. 7 along the central line of holes demonstrate the broadening due to the parallax error and the associated low signal-to-noise ratio for the case of straight drift field lines, as shown in Fig. 8.

While the width of the signal spots from the hole pattern increases with increasing distance from the center of the GEM in the case of a straight drift field, the sharpness of the dots stays the same across the whole width of the GEM when using a radial drift field focused at the source.

A comparison of the two line profiles in Fig. 8 also displays a strong decrease in signal amplitude in the straight drift field configuration, which is less pronounced in the radial drift field configuration. The remaining decrease in signal amplitude in the outer region of the GEM for the case of a radial drift field can be attributed to vignetting introduced by the lens of the CCD camera. For the case of a straight drift field, the broadened signals in off-center regions also display interruptions caused by non-active regions on the GEM due to the 200 μm wide insulating regions between the individual ring-shaped electrodes.

The minimization of the parallax-induced signal broadening is of crucial importance for X-ray fluorescence imaging applications. A Cu grid with horizontal and vertical lines with a pitch of 5 mm was irradiated and excited with 20 keV X-rays to induce characteristic Cu X-ray emission. The emitted fluorescence radiation was imaged with the planispherical GEM detector through a pinhole in the focal point of the radial drift field lines. A comparison of fluorescence images acquired with standard parallel drift field lines and radially focused drift field lines is shown in Fig. 9.

The thick drift region results in significant parallax-induced broadening of the lines of the grid in the image acquired with a standard parallel drift field configuration. This results in strongly limited position resolution in the off-center regions of the detector and makes it hard to distinguish individual vertical grid lines. Switching to radially focused drift field lines, a significantly improved fluorescence image as shown in Fig. 9(b) can be recorded which accurately depicts the grid lines even in the outward regions of the active area and allows the distinction of vertical grid lines.

4. Conclusion

A planispherical GEM detector based on two segmented GEMs and a segmented cathode as well as a drift field shaper was operated to compare the parallax error for straight and radial drift field configurations. The radial field minimizes the parallax error introduced by the uncertainty in the ionization depth in thick drift volumes and results in a correct representation of radially incident X-rays. Fluorescence image quality is significantly improved by radially focused drift field lines with geometric features and signal-to-noise ratio preserved even in off-center regions of the active area of the detector. The planar geometry of the GEMs in the detector is ideally suited for optical readout. The combined features of avoiding the parallax error with a radial drift field and keeping a planar GEM geometry suitable for optical readout permit its use in applications requiring thick drift volumes and good position resolution such as X-ray crystallography or fluorescence. The design can be readily modified to allow for a dynamically tunable focal length of the radial drift field lines by using ring-shaped electrodes with equal widths and tuned sets of resistors in the high voltage divider chains.

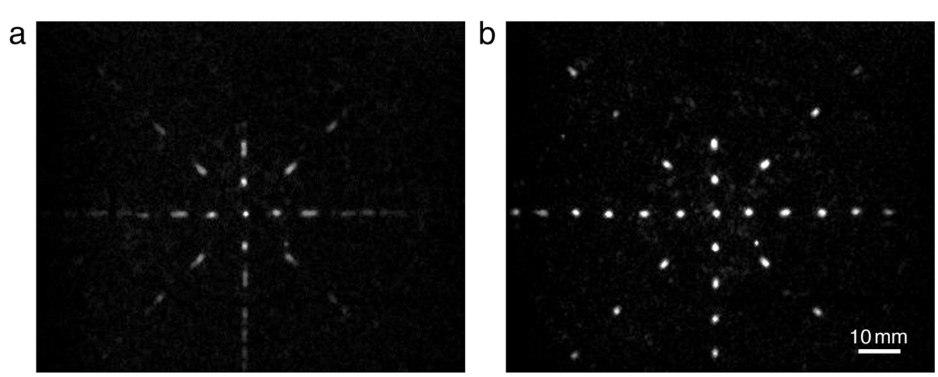

Fig. 7. Images of crosshair hole pattern illuminated with a ^{55}Fe X-ray source in the focal point of the detector. Both images were taken with an exposure time of 100 s and a binning of 8×8 pixels. (a) The image taken with parallel drift field lines perpendicular to the cathode shows the broadening due to the parallax error. (b) Switching to radial drift field lines focused at the source minimizes the parallax error and results in a greatly improved position resolution and signal-to-noise ratio.

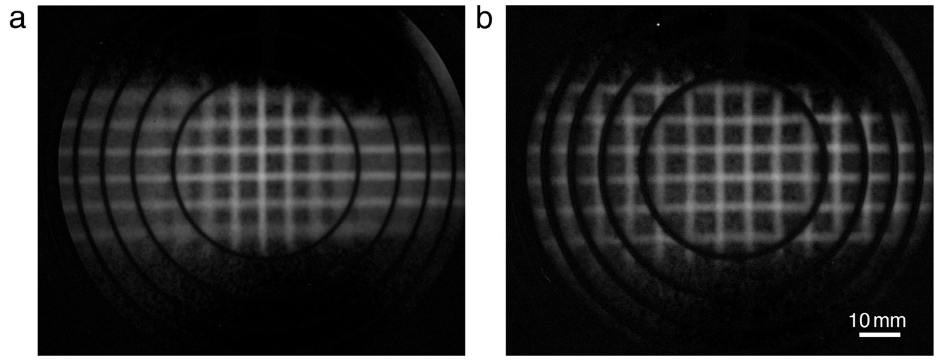

Fig. 9. X-ray fluorescence images of a Cu grid. (a) In the case of parallel drift field lines, the grid lines appear strongly washed out in the outward regions of the active detector area. (b) The radially focused drift field lines of the planispherical GEM allow distinction of grid lines even in the off-center regions of the detector and increase signal-to-noise ratio.

Additionally, switching to a higher number of narrower sectors may minimize nonuniformities caused by unbalanced electron collection close to the insulating gaps between electrodes. The described design can be easily scaled up in size due to the optical readout by a CCD or CMOS camera and provides a convenient way to minimize the effect of the parallax error in MPGD-based detectors.

References

[1] F. Sauli, GEM: A new concept for electron amplification in gas detectors, Nucl. Instrum. Methods Phys. Res. Sect. A. Accel. Spectrometers, Detect. Assoc. Equip. 386 (1997) 531–534. http://dx.doi.org/10.1016/S0168-9002(96)01172-2.

[2] M. Titov, L. Ropelewski, Micro-pattern gaseous detector technologies and Rd51 Collaboration, Mod. Phys. Lett. A 28 (2013) 1–25. http://dx.doi.org/10.1142/S0217732313400221.

[3] M. Bianco, Micromegas detectors for the muon spectrometer upgrade of the ATLAS experiment, Nucl. Instrum. Methods Phys. Res. Sect. A Accel. Spectrometers, Detect. Assoc. Equip. 824 (2016) 496–500. http://dx.doi.org/10.1016/j.nima.2015.11.076.

[4] D. Abbaneo, E. Al, Status report of the upgrade of the CMS muon system with Triple-GEM detectors, Nucl. Instrum. Methods Phys. Res. Sect. A Accel. Spectrometers, Detect. Assoc. Equip. (2015). http://dx.doi.org/10.1016/j.nima.2015.11.125.

[5] D. Pacella, G. Pizzicaroli, M. Leigheb, R. Bellazzini, A. Brez, M. Finkenthal, D. Stutman, B. Blagojevic, R. Vero, R. Kaita, A.L. Roquemore, D. Johnson, Fast x-ray imaging of the national spherical tokamak experiment plasma with a micropattern gas detector based on gas electron multiplier amplifier, Rev. Sci. Instrum. 74 (2003) 2148–2151. http://dx.doi.org/10.1063/1.1537873.

[6] F. Sauli, Radiation imaging with gaseous detectors, Nucl. Instrum. Methods Phys. Res. Sect. A Accel. Spectrometers, Detect. Assoc. Equip. (2017) 1–8. http://dx.doi.org/10.1016/j.nima.2017.01.056.

[7] R.M. Gutierrez, E.A. Cerquera, G. Mañana, MPGD for breast cancer prevention: A high resolution and low dose radiation medical imaging, J. Instrum. 7 (2012). http://dx.doi.org/10.1088/1748-0221/7/07/C07007. C07007–C07007.

[8] N. Pavel, Particle detectors for biomedical applications—demands and trends, Nucl. Instrum. Methods Phys. Res. Sect. A Accel. Spectrometers, Detect. Assoc. Equip. 478 (2002) 1–12. http://dx.doi.org/10.1016/S0168-9002(01)01709-0.

[9] M. Marafini, V. Patera, D. Pinci, A. Sarti, A. Sciubba, E. Spiriti, Optical readout of a triple-GEM detector by means of a CMOS sensor, Nucl. Instrum. Methods Phys. Res. Sect. A Accel. Spectrometers, Detect. Assoc. Equip. (2015) 10–12. http://dx.doi.org/10.1016/j.nima.2015.11.058.

[10] L.M.S. Margato, F.A.F. Fraga, S.T.G. Fetal, M.M.F.R. Fraga, E.F.S. Balau, A. Blanco, R.F. Marques, A.J.P.L. Policarpo, Performance of an optical readout GEM-based TPC, Nucl. Instrum. Methods Phys. Res. Sect. A Accel. Spectrometers, Detect. Assoc. Equip. 535 (2004) 231–235. http://dx.doi.org/10.1016/j.nima.2004.07.126.

[11] A.V. Klyachko, V. Moskvin, D.F. Nichiporov, K.A. Solberg, A GEM-based dose imaging detector with optical readout for proton radiotherapy, Nucl. Instrum. Methods Phys. Res. Sect. A Accel. Spectrometers, Detect. Assoc. Equip. 694 (2012) 271–279. http://dx.doi.org/10.1016/j.nima.2012.08.049.

[12] A. Bressan, R. De Oliveira, A. Gandi, J.C. Labbé, L. Ropelewski, F. Sauli, D. Mörmann, T. Müller, H.J. Simonis, Two-dimensional readout of GEM detectors, Nucl. Instrum. Methods Phys. Res. Sect. A Accel. Spectrometers, Detect. Assoc. Equip. 425 (1999) 254–261. http://dx.doi.org/10.1016/S0168-9002(98)01405-3.

[13] X.-H. Wang, J.-L. Wu, J.-B. Li, Simulation study of the parallax effect of gaseous detectors, Chinese Phys. C. 36 (2012) 1106–1110. http://dx.doi.org/10.1088/1674-1137/36/11/012.

[14] G. Charpak, S. Majewski, F. Sauli, The scintillating drift chamber: A new tool for high-accuracy, very-high-rate particle localization, Nucl. Instrum. Methods. 126 (1975) 381–389. http://dx.doi.org/10.1016/0029-554X(75)90701-6.

[15] E. Aprile, A. Bolotnikov, D. Chen, R. Muhkerjee, F. Xu, Detection of γ-rays with a 3.5 l liquid xenon ionization chamber triggered by the primary scintillation light, Nucl. Instrum. Methods Phys. Res. Sect. A Accel. Spectrometers, Detect. Assoc. Equip. 480 (2002) 636–650. http://dx.doi.org/10.1016/S0168-9002(01)01204-9.

[16] T. Meinschad, L. Ropelewski, F. Sauli, Detection of primary and field-enhanced scintillation in xenon with a CsI-coated GEM detector, Nucl. Instrum. Methods Phys. Res. Sect. A Accel. Spectrometers, Detect. Assoc. Equip. 547 (2005) 342–345. http://dx.doi.org/10.1016/j.nima.2005.03.157.

[17] G. Charpak, Z. Hajduk, A. Jeavons, R. Kahn, R. Stubbs, The spherical drift chamber for X-ray imaging applications, IEEE Trans. Nucl. Sci. 22 (1975) 269–271. http://dx.doi.org/10.1109/TNS.1975.4327649.

[18] R. Kahn, R. Fourme, R. Bosshard, T. Prange, The spherical drift chamber used at LURE for protein crystallography; last developments, performances, and results, Rev. Sci. Instrum. 60 (1989). http://dx.doi.org/10.1063/1.1141036.

[19] S.D. Pinto, M. Alfonsi, I. Brock, G. Croci, E. David, R. De Oliveira, L. Ropelewski, M. Van Stenis, H. Taureg, M. Villa, First results of spherical GEMS, IEEE Nucl. Sci. Symp. Conf. Rec. (2010) 1877–1880. http://dx.doi.org/10.1109/NSSMIC.2010.5874100.

[20] A. Morozov, L.M.S. Margato, M.M.F.R. Fraga, L. Pereira, F.a F. Fraga, Secondary scintillation in CF 4: emission spectra and photon yields for MSGC and GEM, J. Instrum. 7 (2012). http://dx.doi.org/10.1088/1748-0221/7/02/P02008. P02008–P02008.

[21] COMSOL Inc., https://www.comsol.com (accessed May 18, 2017).